JOURNAL OF GEOPHYSICAL RESEARCH, VOL. 102, NO. B11, PAGES 24,639-24,653, NOVEMBER 10, 1997

Present-day plate motion constraint on mantle rheology and convection

Lianxing Wen and Don L. Anderson

Seismological Laboratory, California Institute of Technology, Pasadena

Abstract. Large-scale mantle convection, to first order, is a system driven by interior density anomalies, modulated by variable plate thickness and extreme rheology variations at the top of the mantle. The rheological difference between oceanic and continental regions significantly influences the surface velocity. We apply a three-dimensional Newtonian viscous flow model to explain the large-scale present-day plate motions. The density anomalies are derived from seismic tomography and a slab model. With a viscosity difference of a factor of 30-60 between continents and oceans in the upper 90 km of the Earth, we are able to explain both the observed large-scale poloidal and toroidal plate motions. The viscosity difference between continental and oceanic regions has major control on both the poloidal-toroidal kinematic energy partitioning and the pattern of toroidal motion. Nonlinear rheology can help establish toroidal motion. Plate motions can be explained by assuming either layered or whole mantle flow. In order to match the amplitude of observed plate motions, the value of the reference viscosity (corresponding to that of between 400 to 670 km depth) is 1.6 $\times 10^{21}$ Pa s for layered mantle flow and 3.2 $\times 10^{21}$ Pa s for whole mantle flow. However, the predicted net rotation of the lithosphere, from both layered and whole mantle flow models, is very small and cannot account for the amplitude of the net rotation obtained from the plate tectonic models assuming a fixed hotspot reference frame.

1. Introduction

Plate tectonics is generally believed to be the result of mantle convection. While several large-scale geophysical observables, such as geoid and topography, can be explained in the context of mantle convection [*Hager*, 1984; *Ricard et al.*, 1984; *Hager et al.*, 1985; *Forte et al.*, 1993; *Wen and Anderson*, 1997b], plate motions remain a puzzle for mantle convection. Plate motions are important in many contexts of mantle dynamics,

1. They are the direct evidence of plate tectonics; only after we have established the relationship between observed plate-like motions and mantle convection models can we understand plate tectonics in the context of mantle convection, and vice versa. Figure 1a shows present-day plate motions in the hotspot reference frame from a plate tectonic model [*Gordon and Jurdy*, 1986]. One can decompose these plate motions into poloidal and toroidal motions [*Hager and O'Connell*, 1979], or equivalently, divergence and vorticity [*Forte and Peltier*, 1987]. Figure 1b shows the spherical harmonic $l = 1 - 5$ components of divergence and vorticity obtained from the plate motions shown in Figure 1a. Divergence is defined as $\nabla_H \cdot U$ (U is the surface velocity) and represents convergent (negative) or divergent (positive) motions, and vorticity $(\nabla \times U) \cdot \hat{\mathrm{r}}$ ($\hat{\mathrm{r}}$ is the radial unit vector) represents the shear motions between plates (negative corresponding to clockwise rotation). Models with radial symmetric viscosity structure predict poloidal motions only [*Hager and O'Connell*, 1981]. Models with temperature and stress-dependent viscosity predict a small component of toroidal motion [*Christensen and Harder*, 1991; *Tackley*, 1993; *Cadek et al.*, 1993; *Zhang and Christensen*, 1993]. The observed toroidal/poloidal ratio is close to unity [*O'Connell et al.*, 1991]. Effects on the lateral variation of viscosity in the lithosphere have also been studied by several authors, with approximate methods [e.g., *Ricard et al.*, 1988; *Stewart*, 1992; *Ribe*, 1992]. However, the origin of toroidal plate motion remains unknown.

2. Plate motions are directly related to the question of the complexity of mantle convection. Are plate-like motions controlled by some "magic" behavior of the so-called "plates" which is beyond our modeling ability? Or, are plate-like motions controlled by mantle convection modulated by surface boundary conditions? Are the plates controlled by very special rheology, or is simple rheology sufficient to explain large-scale plate behavior? One approach is to define plate geometries a priori and assume plate-like (either observed or to-be-determined) velocity as a boundary condition, regardless of the origin of these plate velocities [*Hager and O'Connell*, 1981; *Ricard and Vigny*, 1989; *Gable et al.*,

Paper number 97JB02159.
0148-0227/97/97JB-02159$09.00

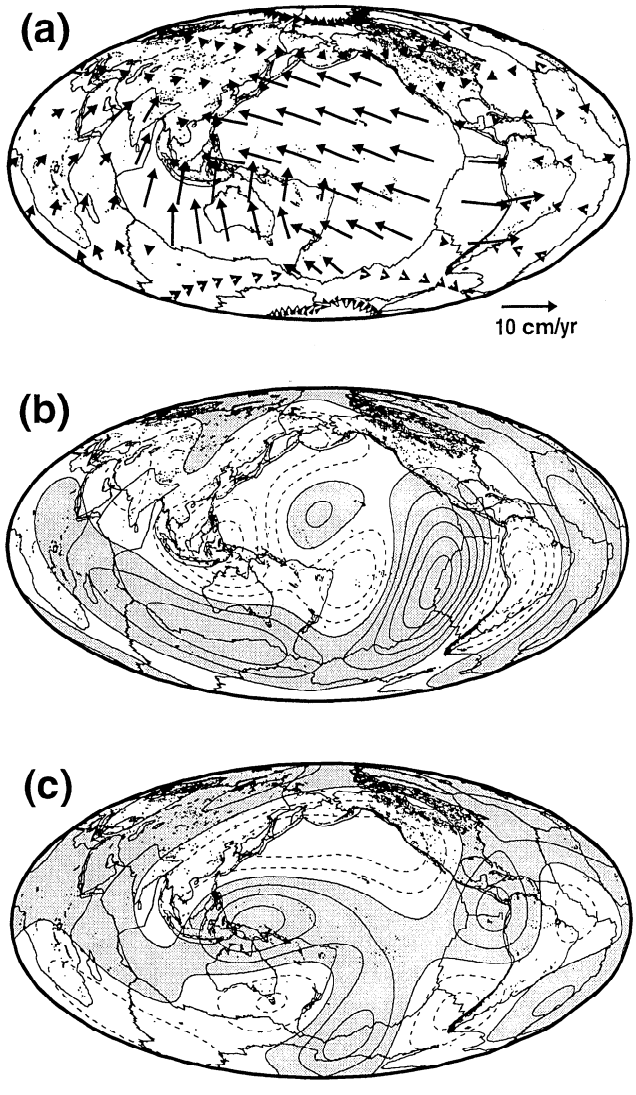

Figure 1. (a) Surface plate velocity, (b) divergence ($l = 1-5$), and (c) vorticity ($l = 2-5$) of surface velocity constructed from the finite rotation poles and angular velocities of *Gordon and Jurdy* [1986] in the hotspot reference frame. See text for the definitions of divergence and vorticity. Positive values of divergence correspond to divergent motion, and negative values correspond to convergent motion. Negative values of vorticity correspond to clockwise rotation, and positive values correspond to counterclockwise rotation. Regions with positive values are shaded. Contour interval is 1×10^{-8} rad/yr.

1991; *Lithgow-Bertelloni and Richards*, 1995]. The constraint is that the forces or torques induced by the interior density anomalies and those caused by the imposed surface velocity are balanced at the surface of the Earth or at a certain depth in the mantle. Lateral variation of viscosity is usually ignored. One problem with this approach is that the total stress acting on the plate, due to the imposed plate-like velocity, goes to infinity [*Hager and O'Connell*, 1981]. One way around this dilemma is to balance the torques at a certain depth in the mantle [*Hager and O'Connell*, 1981; *Gable et al.*, 1991]. However, the normal forces between plates and the average shear stress at the surface still go to infinity. Another way to deal with this problem is to apply a failure criterion for the lithosphere and mathematically truncate the stress contribution at a certain harmonic degree [*Ricard and Vigny*, 1989; *Lithgow-Bertelloni and Richards*, 1995]. Plates are essentially partly moved with "the finger of God" in this approach. Another approach is to invoke special rheology for the lithosphere to explain the observed plate motions. For example, *Bercovici* [1993, 1996] argues that lithosphere might have a special rheology with dynamic self-lubrication in order to produce plate-like motions. *O'Connell et al.* [1991] and *Olsen and Bercovici* [1991] attribute the kinematic partition of toroidal and poloidal motions to the geometrical effects of the existing plates. On other hand, *Zhong and Gurnis* [1995, 1996] suppose that preexisting faulted plate margins hold the key to the present-day plate motions.

3. Plate motions provide important constraints on surface rheology. Unlike geoid and topography, which place strong constraints on the radial viscosity structure, plate motions place constraints more strongly on the lateral variation of viscosity. For example, weak plate margins [*Lachenbruch and Sass*, 1988] may have a large influence on plate motions, based on two-dimensional flow models [*Gurnis*, 1989]. *Ribe* [1992] predicts a substantial toroidal component of surface motions by considering a model in which the lithosphere is represented as a thin shell with laterally variable thickness, overlaying a radially symmetric mantle. *O'Connell et al.* [1991] and *Ricard et al.* [1991] claim that at least 1 order magnitude of difference of viscosity between continental and oceanic mantle is required to explain the observed net rotation ($l = 1$ toroidal motion) of the lithosphere in a fixed hotspot reference frame. Plate motions can also place constraints on the absolute value of viscosity in the mantle, whereas geoid and topography can only constrain the relative values of viscosity.

It is also worth mentioning that toroidal surface motion is essentially a three-dimensional problem. Any two-dimensional investigations of lateral variation of viscosity [e.g., *Richards and Hager*, 1989] would have limited application in modeling the toroidal motions in three dimensions. Three-dimensional models can also be constrained by geoid and topography. In this paper we present a new method to calculate three-dimensional Newtonian flow with lateral variable viscosity and test several rheological models for their capability of generating toroidal motions. In the first section we discuss briefly the new method and present several rheological models for a simple slab density model. We will focus on rheological models with large-scale variations, that is, rheological differences between continental and oceanic regions. In the second section we refine the density model to match geoid and surface residual topography [*Cazenave et al.*, 1989]. The density anomalies are derived from residual tomography [*Wen and Anderson*,

1997a] and the presence of slabs in the upper mantle and seismic tomography [*Su et al.*, 1994] in the lower mantle. The predicted plate velocities are presented. We also discuss the net rotation of the lithosphere.

2. Three-Dimensional Newtonian Flow and Model Experiments

2.1. Method

Earth's mantle is assumed to behave as an incompressible Newtonian viscous fluid with negligible Reynolds number. Three sets of equations govern the mantle flow:
Equation of continuity

$$\nabla \cdot U = 0, \tag{1}$$

where U is the velocity.
Equations of motion at zero Reynolds number

$$\nabla \cdot \tau + \delta\rho g = 0, \tag{2}$$

where τ is the stress tensor, $\delta\rho$ the density anomaly and g the gravitational acceleration.
Constitutive equation for Newtonian flow

$$\tau = -p + 2\eta\varepsilon, \tag{3}$$

where p is the pressure, η the viscosity and ε the strain rate tensor.

The appendix gives procedures for solving these equations in spherical coordinates. The horizontal variations of variables are expressed in terms of spherical harmonics. For a radially symmetric viscosity structure, toroidal-poloidal, poloidal-poloidal and toroidal-toroidal equations, are decoupled at every spherical harmonic degree and order [*Kaula*, 1975; *Hager and O'Connell*, 1981]. For a structure with lateral viscosity contrast, toroidal and poloidal equations are coupled and equations at every degree or order of the spherical harmonics are also coupled with each other. The coupling coefficients are presented in the appendix. If we truncate the contribution at a certain spherical harmonic degree ($l_{\max}$) and consider the coupling effects for those spherical harmonic degrees ($l \leq l_{\max}$), we can reduce the above three set of equations to a set of linear equations. These linear equations have constant coefficients for a shell with the same form of lateral variation of viscosity and can be solved by standard propagator matrices [*Gantmacher*, 1960] (see appendix for details). The geoid and dynamic topography at various boundaries in the mantle can be easily obtained from Z_3^{lm} terms in the appendix. The procedures of obtaining geoid and topography are presented elsewhere.

The method has been checked by the following procedures:

1. For radially symmetric viscosity, the solutions are in exact agreement with those obtained by traditional propagator matrix method [e.g., *Hager and O'Connell*, 1981].

2. We compare our results with those obtained by the method of *Zhang and Christensen* [1993] for the density perturbation $\delta\rho = \sin \pi z * Y_{11} + Y_{20}$ and viscosity structure $\eta = \eta_0 \exp(C * \delta\rho)$, where $C = 0.2$, $z = (r - r_i)/(r_0 - r_i)$, r_0 and r_i are the radii of the Earth's surface and the core-mantle boundary, and η_0 is the reference viscosity, and $Y_{11}, Y_{2,0}$ are the normalized spherical harmonics. The correlation coefficients between predicted divergence and vorticity by the two methods are shown in Figure 2a and the normalized spectra of predicted divergence and vorticity are shown in Figure 2b. The results obtained by the two methods are in excellent agreement.

3. We compare our large-scale predictions of divergence and vorticity with those obtained by *Ribe* [1992] for a three plate model with lateral variation of viscosity in a shell. For comparison, we assume that the lateral variation of viscosity is confined in a thin shell with a thickness of 10 km and the rest of the mantle

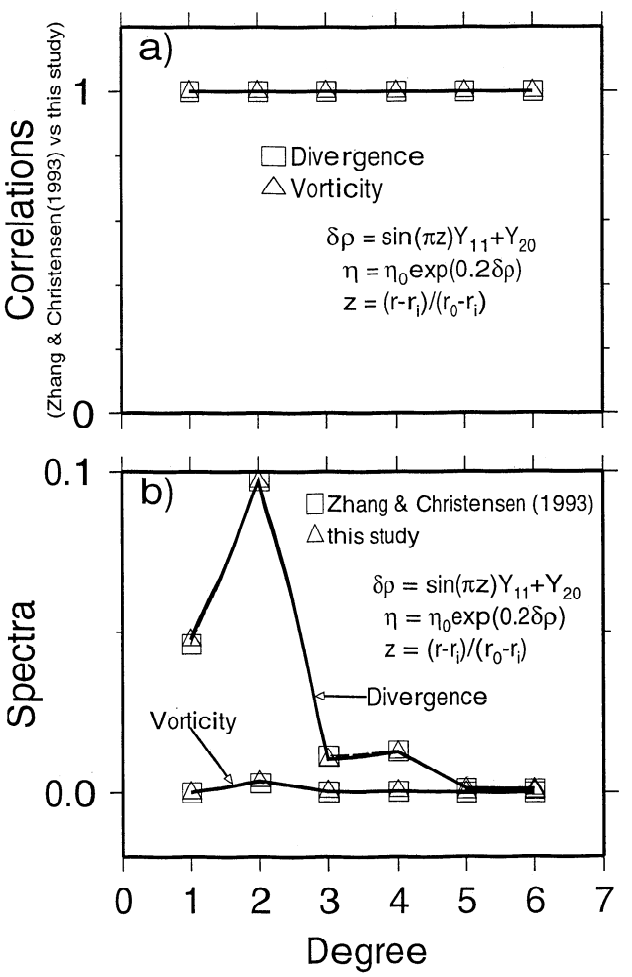

Figure 2. Comparisons between the results produced by the method of *Zhang and Christensen* [1993] and those obtained by this study. The distributions of density anomalies and viscosity are shown in the figures. (a) Correlation coefficients between the predictions by two methods and (b) comparison of spectra obtained by two methods.

has uniform viscosity 1. Figure 3a shows the lateral variation of viscosity in the thin shell or the "stiffness" $f = (h/a)(\eta(\theta,\phi)/\eta(a)-1)$, as defined by *Ribe* [1992], as a function of colatitude. The "stiffness" is scaled from the lateral variation of viscosity, and $\eta(\theta,\phi)$ is the viscosity in the shell, $\eta(a)$ is the reference viscosity, h is the thickness of the shell and a is the radius of the Earth. The variation of this "stiffness" is very similar to that used by *Ribe* [1992]. Mantle flow is driven by a surface density contrast of degree and order $(l,m) = (2,\pm1)$ in the middle mantle ($r = 0.773a$). The predicted divergence along the meridian $\phi = 0$ and vorticity along the meridian $\phi = 90^0$ are shown in Figures 3b and 3c. A truncation degree of $l_{\max}$= 12 is used in our calculation and a truncation degree of $l_{\max}$= 128 is used by *Ribe* [1992]. Thus small-scale features are missing in our results. Note, however, that at long wavelengths, we obtain very good agreement between the two methods (see Figure 8 of *Ribe* [1992]).

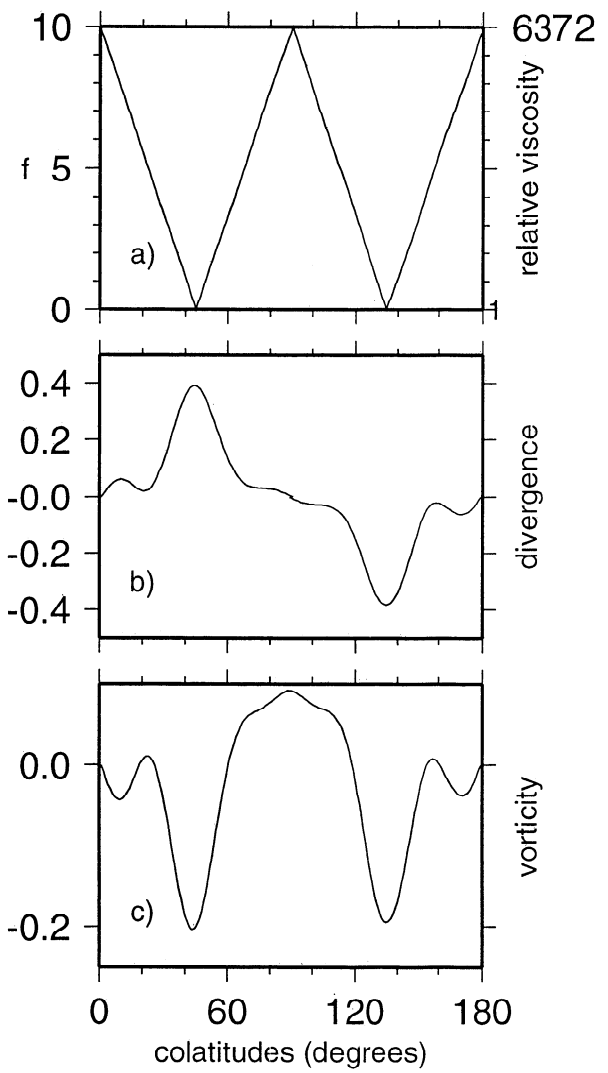

Figure 3. Effects of large lateral variations on the surface velocity field, for a three-plate model, as defined by *Ribe* [1992]. (a) "Stiffness" $f(\theta)$ or relative viscosity in a thin shell of thickness of 10 km, (b) profile of surface divergence along the meridian $\phi = 0$, and (c) profile of radial vorticity along the meridian $\phi = 90^0$. Surface divergence and radial vorticity are shown in units of $g\sigma/\eta_0$. The flow is driven by a surface density contrast of degree and order $(2,\pm1)$ in the middle mantle (see Figure 8 of *Ribe* [1992] for comparison).

2.2. Thermal Models

2.2.1. Oceanic lithosphere. Several models have been proposed to explain the heat flow and bathymetry data in the oceanic regions. The increase in ocean depth away from spreading centers varies linearly, on average, with the square root of age of the oceanic plates up to 70-80 m.y. [*Parsons and Sclater*, 1977], as predicted by both the half-space cooling model [*Turcotte and Oxburgh*, 1967] and the plate model [*Parsons and Sclater*, 1977; *Stein and Stein*, 1992]. The plate model can fit the average ocean data beyond 70-80 m.y. Many mechanisms have been proposed to explain the departure of the observed ocean depth from the trend predicted by the half-space cooling model. For example, small-scale convection [*Richter*, 1973], hotspots [*Heestand and Crough*, 1981], viscous heating [*Schubert et al.*, 1976], etc. For the purpose of our study the differences between these models are rather small. The forces generated by the cooling of oceanic lithosphere are small compared to those resulting from density variations in the mantle. The plate model of *Stein and Stein* [1992] is used in the oceanic regions. The temperature $T(x,z)$ as a function of distance x from the ridge and depth z below the seafloor is given by

$$T(x,z) = T_m[z/a + \sum_{n=1}^{\infty} c_n \exp(-\beta_n x/a)\sin(n\pi z/a)],$$

where a is plate thickness (95 km), T_m is basal temperature (1450° C) and

$$c_n = 2/(n\pi),\ \beta_n = (R^2 + n^2\pi^2)^{1/2} - R,\ R = va/(2\kappa),$$

where thermal diffusivity $\kappa = k/(\rho_m C_p)$, k is thermal conductivity (7.5×10^{-3} cal K^{-1} cm^{-1} s^{-1}), ρ_m is mantle density (3330 kg m^{-3}) and C_p is specific heat (0.28 cal g^{-1} K^{-1}). The thermal expansion coefficient $\alpha = 3.28\times10^{-5}$ K^{-1} and the digital ocean age map by *Müller et al.* [1993] are used. Continents are assumed to be equivalent to ridges in terms of density in the upper 90 km. The upper 90 km is divided into nine layers each with thickness of 10 km.

2.2.2. Density anomalies in the mantle. The density anomalies in the mantle are assumed to be only those related to subducting slabs. The locations of slabs are shown in Figure 4. Slabs are assigned a thickness of 128 km and density contrast of 0.067 g/cm^3, regardless of age. They are assumed to sink vertically into the mantle and to be confined to the upper mantle. This slab model is expanded into spherical harmonic degrees.

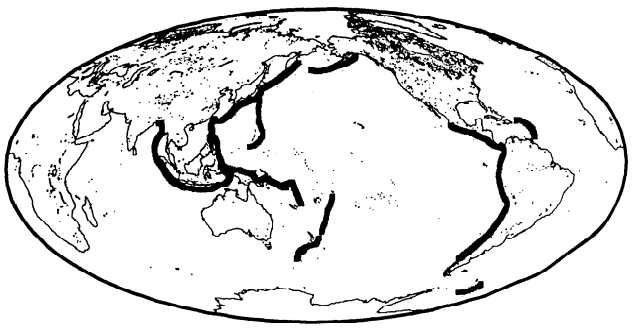

Figure 4. Locations of present-day subduction zones.

The upper mantle is divided into 11 layers of thickness 50 km. This density model in no way represents all the thermal anomalies in the real Earth. However, it can be used to test the viscosity structure of the mantle at high spherical harmonics.

2.3. Viscosity Structure of the Earth

Several mechanisms may cause lateral variations in viscosity: (1) temperature dependence, (2) stress dependence, and (3) chemical differences. Models of mantle flow with temperature-dependent viscosity in a three-dimensional Cartesian geometry [*Christensen and Harder*, 1991; *Tackley*, 1993] and spherical geometry [*Zhang and Christensen*, 1993] and with stress-dependent viscosity [*Cadek et al.*, 1993; *Zhang and Christensen*, 1993] are unable to generate sufficient toroidal energy to be compatible with the observations. In this study we consider temperature- and stress-dependent viscosity to be second-order effects in generating toroidal plate motions at the surface. The extreme lateral variations in viscosity probably occur at shallow depths, where the rheological difference of continental and oceanic regions is obvious. Figure 5 shows the regionalization of continents, oceans and plate margins in the present-day configuration. We assume viscosity variation exists only in the upper 90 km; the rest of the mantle has radially symmetric viscosity structure. To resolve weak plate margins might require a very high truncation degree in spherical harmonic domain, which is very difficult for our technique to handle. Note that the number of linear equations grows as $l^2_{\max}$ and the calculation grows as $l^6_{\max}$. Thus we will focus on testing rheological models with long-wavelength variations in viscosity. One obvious candidate is the rheological difference between oceanic and continental regions, as is obvious from seismic images [e.g., *Zhang and Tanimoto*, 1993; *Grand*, 1994; *Polet and Anderson*, 1995]. All the calculations will be done with truncation degree $l_{\max}$= 12, and we will only consider the components of degrees ($l \leq 5$), since they are affected very little by neglecting the coupling effects of small-scale structures, as we will show later.

We start from a very simple model with stiff "continents" overlaying a uniform mantle. "Continents" include thick cold cratons as well as noncratonic areas. They also include crust and upper mantle. "Continents," however, are assumed to have uniform viscosity and uniform thickness (90 km). Thus lateral variations in viscosity exist only in the upper 90 km of the mantle. The schematic representation of the viscosity structure is shown in Figure 6a. The predicted toroidal/poloidal spectrum ratios for this model reach about 40%. However, no significant correlations between predicted and observed vorticity are found (Figure 6a). Figure 6b shows results for a model similar to model a but with a stiff lower mantle (model b). Model b predicts less toroidal motion, but the correlation becomes better at degree l = 6. Overall, a high-viscosity lower mantle has little effect on the prediction of plate motions. The toroidal energy predicted by models a and b cannot account for the observations.

Significant changes appear for the model (model c) with a weak asthenosphere (Figure 6c), which is simulated as a channel with low viscosity. Plates are decoupled efficiently from the rest of the mantle through this weak asthenosphere. Significant toroidal plate motions are predicted. As shown in Figure 6c, the toroidal/poloidal spectrum ratios are around 0.8-1.2, very close to observations. The predicted and observed vorticity patterns correlate well at degrees $l = 2 - 6$. The above model experiments indicate that plates with a viscosity difference between continental and oceanic regions can be driven by the cooling of the oceanic plates and subducting slabs and can move in the right direction, if they are efficiently decoupled from the rest of the mantle. Both the viscosity difference of the continental and oceanic regions and a low-viscosity asthenosphere are important in generating plate motions at the Earth's surface.

2.4. Truncation Effects

The coupling effects among spherical harmonic degrees $l < l_{\max}$ are exactly predicted by our method, but the effects of small-scale structures on the large-scale predictions are still unknown. It is worthwhile investigating the effects of using different truncation degrees ($l_{\max}$). Very little change in the prediction

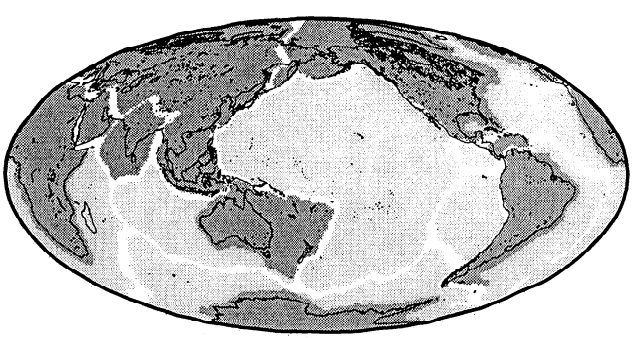

Figure 5. Regionalization of tectonic regions. The upper 90 km is divided into three regions: oceans (light gray), plate margins (white), and continents (dark gray).

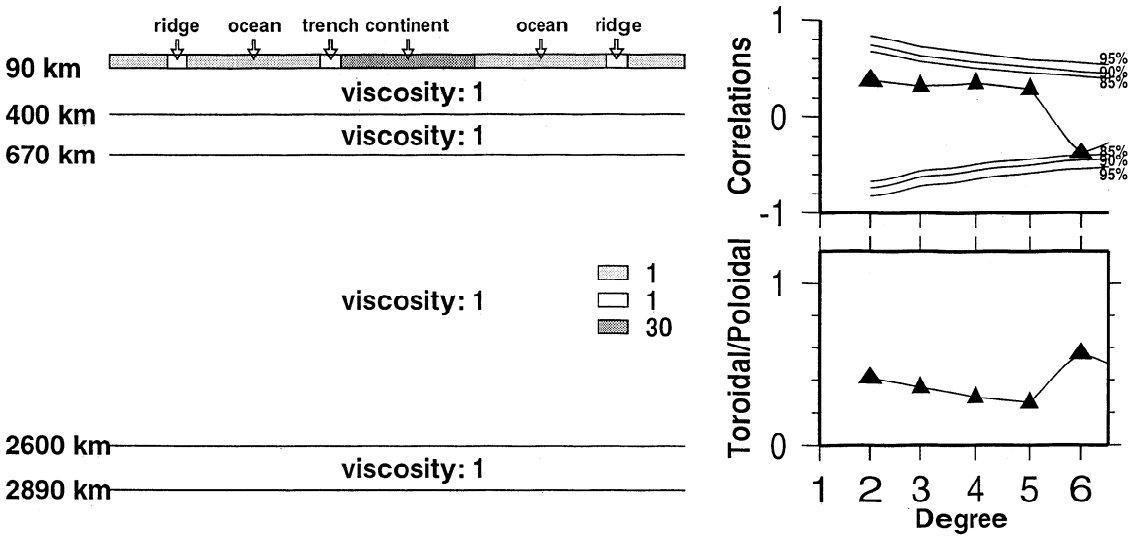

Figure 6a. Viscosity model for model a, where uniform viscosity mantle is overlain by stiff continents: (right bottom) ratio of predicted spectra of surface toroidal to poloidal motions; (right top) correlation coefficients of predicted and observed vorticity. The buoyancy forces are assumed to be slabs only.

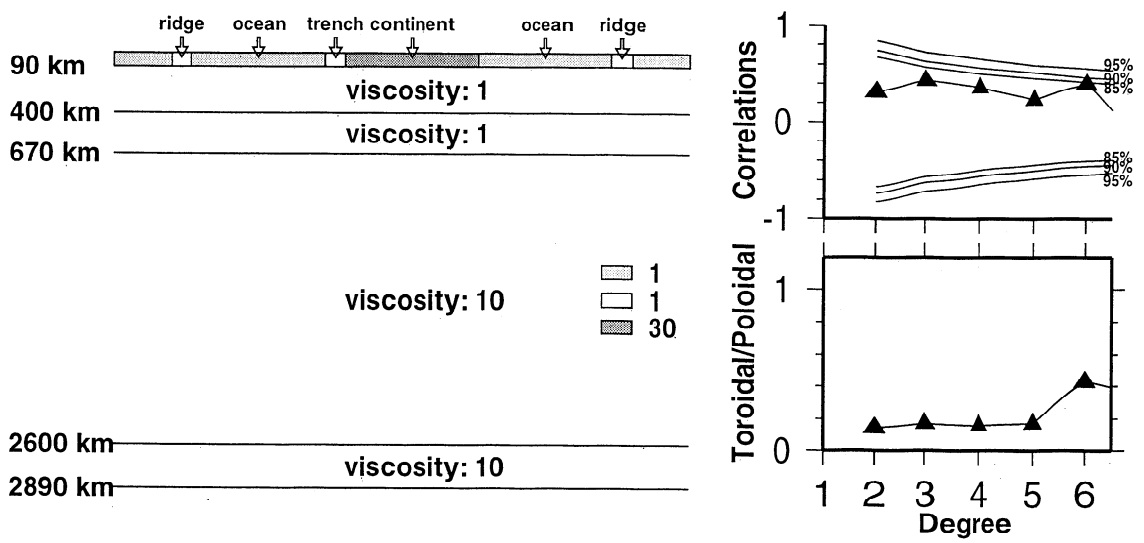

Figure 6b. Same as Figure 6a, except for model b, which has a high-viscosity lower mantle.

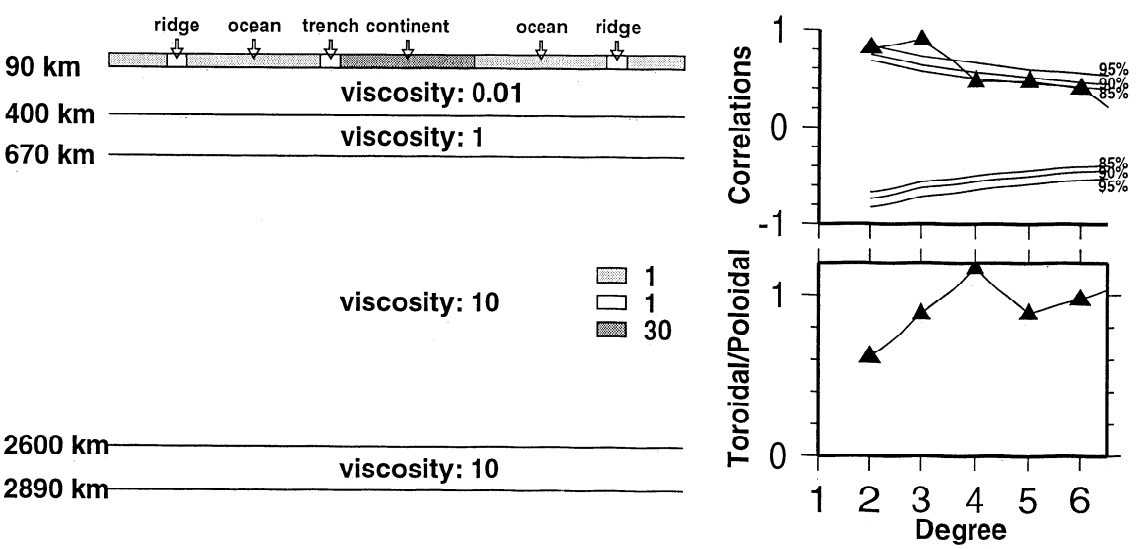

Figure 6c. Same as Figure 6a, except for model c, which has a high-viscosity lower mantle and a weak asthenosphere below the lithosphere. Note the ratio of predicted spectra of toroidal/poloidal velocities and the good correlations between predicted and observed vorticity.

of models a-c is observed. Figure 7 shows the correlation coefficients and percentage change of spectrum between the predicted divergence and vorticity with truncation degree l_{max}= 12 for model c and those with different truncation degrees. The predictions at two extreme degrees (l = 1, 5) are shown. The correlation coefficients are between 0.99 and 1 for both divergence and vorticity, and the spectra have about a maximum of 4% variations. This experiment indicates that, for the viscosity structure we consider, the density anomalies at 12 < $l_{max}\leq$ 24 contribute very little to the large-scale divergence and vorticity. It is not surprising that the couplings between small-scale density anomalies and small-scale viscosity variation to the large-scale surface velocity are rather small because the power of both density anomalies and lateral variation of viscosity decrease rapidly with spherical harmonic degree l. It should be mentioned that the slab model has smaller scale structures than the tomographic models. The truncation effects are expected to be smaller for the real Earth. Considering the uncertainties of the density model, we believe that the prediction with truncation degree l_{max}= 12, the highest degree of our density (tomographic) model, is good enough and will be robust for predicting the plate velocities at degrees $l = 1 - 5$. For the purpose of mimicking the large-scale effects of stress-dependent viscosity, we will include "weak zones" in the plate margins in the following calculations. It should be mentioned that truncation effects are larger for purely "weak zones" models than for "ocean/continent" models. The purpose here is purely for mimicking the stress-dependent viscosity, since stresses are likely to be large at plate margins and will decrease the effective viscosities. Equivalently, we impose a gradient of stress-dependent viscosity variation by truncating "weak zones" at low degree.

3. Geoid, Topography, and Plate Motion Constrained Mantle Convection

In this section we refine our density model to fit the geoid and residual topography.

3.1. Refined Density Anomalies in the Mantle

The long-wavelength ($l = 2-3$) geoid and residual topography [*Cazenave et al.*, 1989] are explained successfully by a density model derived from residual tomography [*Wen and Anderson*, 1997a] in the upper mantle and seismic tomography in the lower mantle for layered mantle flow [*Wen and Anderson*, 1997b]. The amplitude of residual topography places strong constraints on the velocity-density scaling in the shallow mantle. We apply the same velocity-density scalings shown in our previous model at $l = 2 - 3$. At degrees $l = 4 - 9$, geoid and velocity divergence correlate strongly with subducting slabs [*Hager*, 1984; *Forte and Peltier*, 1991]. These slab signals in the upper mantle are missing in the current generation of seismic tomography [*Forte and Peltier*, 1991]. The predictions of geoid and surface velocity divergence based on seismic tomography are generally not good at those degrees. The density anomalies in subducting slabs are somewhat uncertain. We derive a hybrid density model in the upper mantle by adjusting the relative weights of density anomalies of subducting

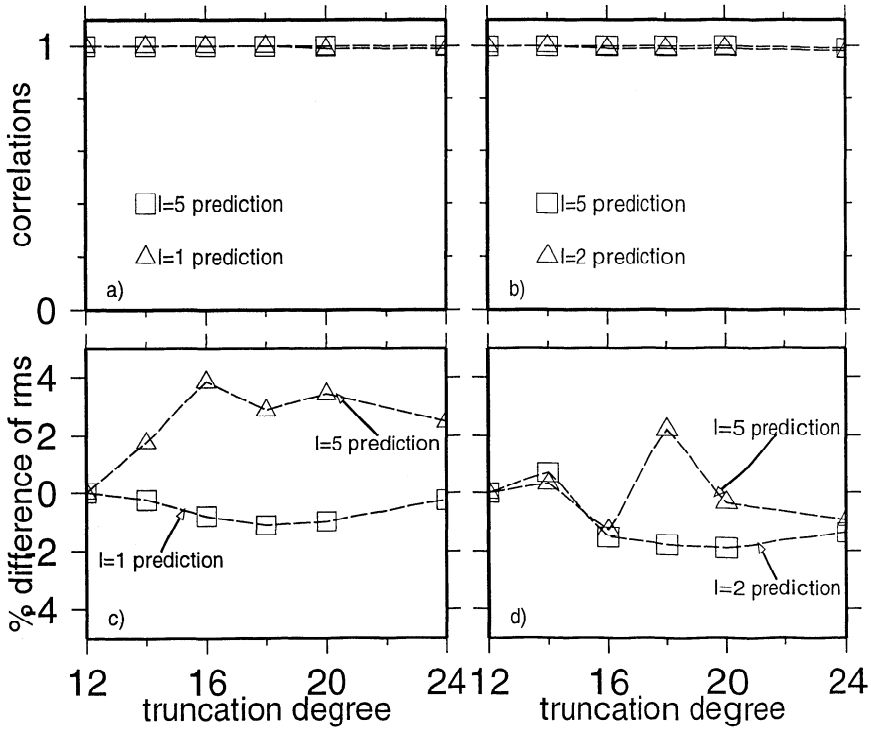

Figure 7. Correlations and rms difference with respect to predicted (left) divergence and (right) vorticity using truncation degree (l_{max} = 12) for those with different truncation degrees.

slabs and residual seismic tomography. This is similar to the approach of *Forte and Peltier* [1991], except that the residual tomography is used in the upper mantle in our approach. Our criterion for choice of parameters for the density models is to match the geoid, residual topography and surface velocity divergence with the observations. We need to test whether we can match the surface vorticity for a given viscosity structure, in terms of magnitude and pattern.

The velocity-density scalings for degrees $l = 4-12$ are shown in Figure 8. The subducting slabs are assumed to sink vertically into the upper mantle and to be confined in the upper mantle (the dip angle of subducting slab is of little consequence at large scale; however, it does modify the inferred thickness of the slab, which, equivalently, is considered by changing the density contrast of the slab). The thickness of subducting slabs is assumed to be 128 km, corresponding to the thickness of a vertically sinking mature slab. The density contrasts in different subduction zones are listed in Table 1. The degree $l = 4 - 12$ components of this slab model are used.

The Earth is divided into 43 layers: 9 layers in the upper 90 km with thickness of 10 km, 12 layers in the rest of the upper mantle, and 22 layers in the lower mantle. We test two models for mantle convection: layered mantle and whole mantle flow. Again, all the calculations are done with truncation degree $l_{max}= 12$ and only prediction at degrees $l = 1 - 5$ will be discussed.

3.2. Buoyancy Driven Plate Motions

The layered mantle convection model used here is the same as we used in explaining the long-wavelength geoid and residual surface topography [*Wen and Anderson*, 1997b], except that now there is strong lateral variation of viscosity in the upper 90 km of the mantle. The schematic representation of viscosity structure is shown in Figure 9, where both the viscosity contrast between continental and oceanic regions and "weak zones" are considered. The magnitude of the viscosity contrast between continental and oceanic regions is chosen by matching the ratio of the predicted vorticity and divergence to those observed. Mantle flow is assumed stratified at 920 km, rather than at 670 km. There is little difference in this case, however, for the present purposes.

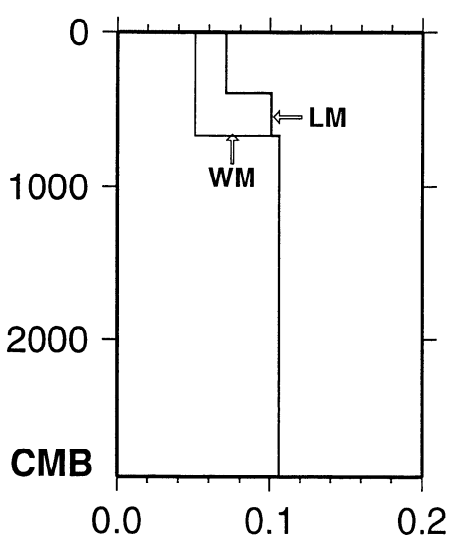

Figure 8. Velocity-density scalings at $l = 4 - 12$ for models assuming layered mantle flow (LM) and whole mantle flow (WM). These scalings for model LM are obtained by matching the amplitude of observed geoid and residual topography; and those for model WM are obtained by matching the amplitude of geoid only.

Table 1. Density Contrast of Slabs

Subduction Zone	LM	WM
Java	32	18
New Hebrides	118	80
Tonga	16	64
Mariana	32	18
Ryukyu	45	18
Kurile	45	18
Aleutian	45	45
Middle America	32	64
Caribbean	32	64
Peru-Chile	110	96

units 10^{-3} g/cm^3.

The predicted divergence and vorticity of surface velocity (Figures 10a-10c) agree well with the observations. The divergent motions at ridges and convergent motions at subduction zones and the magnitudes of those rates are well predicted (see Figure 1b). The clockwise rotation along the San Andreas fault, Aleutian trench, Ryukyu-Kurile trench, south of south America and South Africa and counter-clockwise rotation in north Australia, boundary between North America and Cocos plates and circum-Pacific regions and the magnitude of those rotations are also well predicted by our model. The correlation coefficients between predicted surface divergence and vorticity with those observed are shown in Figure 11. There are good correlations up to $l = 10$ for surface divergence, up to $l = 6$ for surface vorticity. The breakdown at degree $l = 6$ could be due to the neglect of density anomalies at degrees $l > 12$. Since vorticity results from coupling of modes and divergence is mostly caused by the density at the same mode, truncation affects the prediction of vorticity more than that of divergence. The reference viscosity (corresponding to the viscosity in 400 - 670 km depth interval) is 1.6 $\times 10^{21}$ Pa s for the layered mantle flow model.

The predicted divergence and vorticity assuming whole mantle flow are also shown in Figures 10b and 10d. The density contrasts in different subduction zones are listed in Table 1 and the velocity-density scalings are shown in Figure 8. This density model is only con-

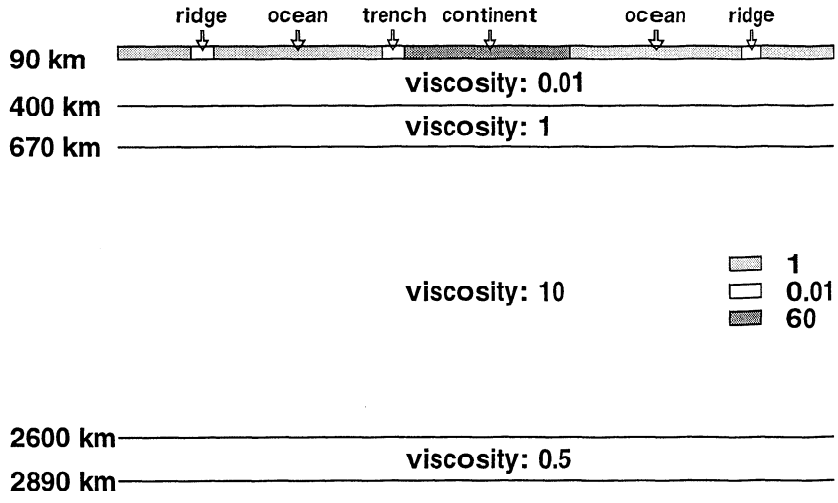

Figure 9. Viscosity model used to predict surface velocity field, assuming layered mantle flow, stratified at 920 km. For the model assuming whole mantle flow, the relative effective viscosity of "continents" is 30.

strained by geoid data. The predictions do not match the observations as well as those assuming layered mantle flow. This is because significant contribution comes from density anomalies in the lower mantle, which have less correlation with the surface divergence. Of course, one can argue that seismic tomography in the lower mantle suffers the same problem as those we claim in the upper mantle, and one can apply the same corrections as we do in the upper mantle. One can probably find a different viscosity structure to make the surface velocity more sensitive to the upper mantle anomalies. The fitting of divergence and vorticity can then be improved significantly. The magnitude of the predicted surface velocity does not constrain the style of mantle convection since it is scaled by the reference viscosity, which is not known exactly. The relative viscosity of "continents" (top of the upper mantle) with respect to that of "oceans" is chosen to be 30 in order to match the power of toroidal and poloidal motions. The reference viscosity is now 3.2×10^{21} Pa s, twice that which was used for layered mantle flow model.

The poloidal and toroidal velocity kernels are shown in Figure 12 for the viscosity structures used to predict the divergence and vorticity in Figure 10. Those kernels represent the responses of surface poloidal and toroidal motions at certain spherical harmonic degrees and orders for a $Y_{2,0}$ load at a certain depth. Only responses at some modes are shown in the figure as an illustration. Besides a pronounced contribution to $Y_{2,0}$ divergence, significant contributions can also be found at other modes. On the other hand, little contribution is found at degree $l = 2$ for vorticity. Significant contributions come from the density anomalies in the upper mantle region for both layered mantle and whole mantle flow models.

It should be clarified that, in the above models, it is the viscosity difference between continental and oceanic regions, not the "weak zones," that controls the main feature of the predictions. Figure 13 shows the predicted surface divergence and vorticity for the density and viscosity models, used in Figures 10a and 10c, except that no "weak zones" are included. The main features of observed vorticity are well predicted, although the correlations between observations and predictions are slightly lower than those from models with weak plate margins. Models with "weak zones," with this truncation degree l_{max}= 12, only predict a small portion of the observed vorticity.

3.3. Net Rotation of the Lithosphere?

The plate reconstruction models by *Gordon and Jurdy* [1986] and model AM1-2 by *Minster and Jordan* [1978] are based on the assumption that hotspots are fixed and they use the hotspot reference frame. There are significant net rotation motions of lithosphere with respect to hotspots for both models. The net rotation reaches 0.11 degree/m.y. around a pole situated at 37°E and 40°S for the model by *Gordon and Jurdy* [1986] and 0.26 degree/m.y. around 68°E and 53°S for the model AM1-2 [*Minster and Jordan*, 1978]. This differential net rotation is sometimes interpreted as the net rotation of the lithosphere with respect to the lower mantle.

The rigid body rotation of the Earth is unconstrained by viscous flow. However, the differential net rotation of Earth's surface with respect to other parts of the mantle is constrained. The predicted net rotation (degree $l = 1$ component of toroidal motion) of the lithosphere with respect to the core-mantle boundary for each model used in Figure 10 is very small (about 1% of observed net rotation with respect to hotspots). This is also true for the net rotation of the lithosphere with respect to other internal boundaries in the mantle and for the convection models assuming layered mantle or whole mantle flow. The predicted net rotation certainly depends on the viscosity models. The lateral variation of viscosity in the deep mantle will have significant ef-

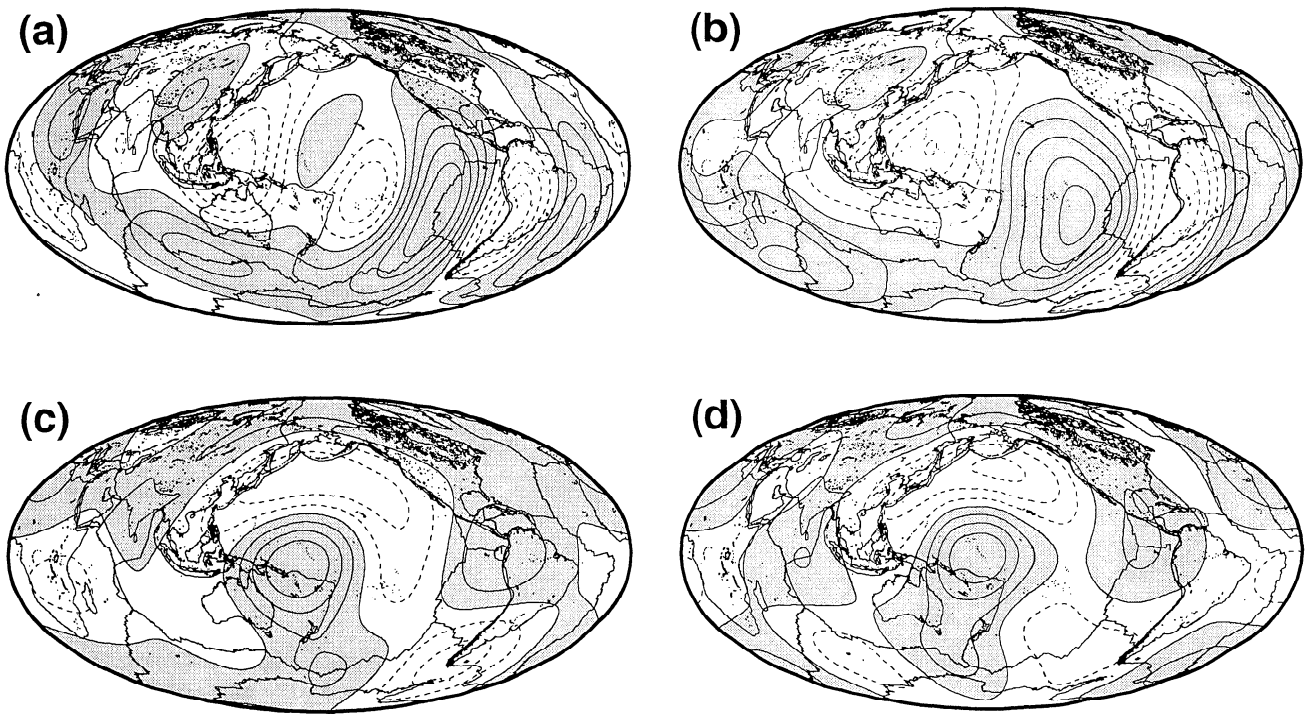

Figure 10. Predicted divergence ($l = 1 - 5$) and vorticity ($l = 2 - 5$) for surface velocity field for models assuming layered (LM) and whole (WM) mantle flow. Regions with positive values are shaded. Contour interval is 1 $\times 10^{-8}$ rad/yr.

fects on the net rotation of the Earth's outer shell. It is unclear, at this stage, whether temperature- and stress-dependent rheology in the deep mantle can produce the net rotation of the Earth's surface, as observed in the hotspot reference frame, or whether the concept of fixed hotspots is in error.

4. Discussion

Although large-scale observed poloidal and toroidal plate motions are well predicted by our model, we have ignored such effects as temperature-dependent viscosity, nonlinear rheology and compressibility in the deep mantle. The lateral variations of viscosity in the deep mantle will certainly affect the prediction, although they are unlikely to be very important in predicting surface plate motions [*Zhang and Christensen*, 1993]. It should also be kept in mind that our model is simplified. For example, the thickness of the plate is purely an assumption, and there are many possible explanations about the causes of the rheological difference between continental and oceanic regions:

1. The viscosity difference between continental and oceanic regions shown in our model could be a reflection of different depths of the lithosphere beneath continental and oceanic regions. The viscosity contrast between continental and oceanic regions is the integrated effect of crust and top of the upper mantle.

2. The viscosity difference between continental and oceanic regions could be the effects of presence of cratons in the continental regions (integrated effects of cratons and younger areas). Cratons appear cold and extend deep in the mantle [*Polet and Anderson*, 1995]. They also affect temperatures and convection in the underlying mantle. Future study on short-wavelength plate motions might help distinguish this possibility.

3. The viscosity beneath continental regions is large compared with that beneath oceanic regions. Viscosity is controlled by composition, temperature, volatile content, and extent of partial melting. It is unclear, at this stage, how those factors affect viscosity.

Although the interpretation of our results has ambiguities, the viscosity contrast between continental and oceanic regions is necessary to produce the correct pattern of toroidal plate motions. We tested rheological model with oceans having 60 times higher viscosity than continents. Not only are no correlations found between predicted and observed vorticity, but correlations between predicted and observed divergence are degraded significantly.

It is important, for the study of mantle convection, to take into account a realistic distribution of surface geology and density anomalies. Despite the simplicity of our model, it can provide considerable insight into some important aspects of the study of the mantle convection:

1. The shallow mantle seems to be very important in controlling mantle dynamics. Density anomalies at shallow depths contribute significantly both to plate velocity (Figure 12) and dynamic surface topography [*Wen and Anderson*, 1997b]. The lateral variations

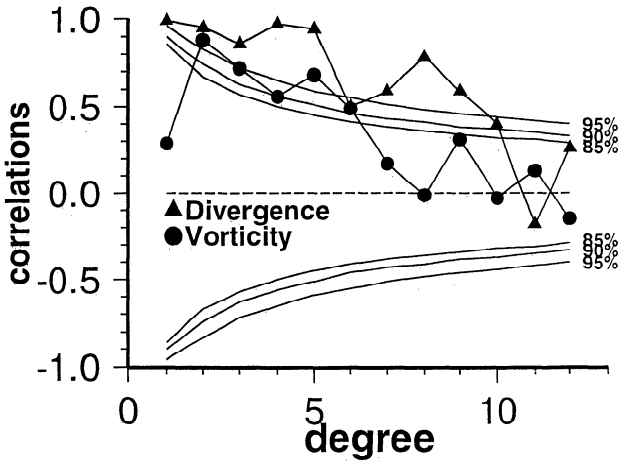

Figure 11. Correlation coefficients between observed divergence and vorticity and those predicted for model LM, assuming layered mantle flow.

of viscosity at shallow depths appear to be important in controlling the plate velocity at the surface of Earth. The complexity of the shallow mantle still needs to be sorted out.

2. Large-scale plate motions can be explained in terms of mantle convection with simple rheologies. The observed plate motions are controlled by mantle rheology and should not be treated as boundary conditions in modeling of mantle convection. With improving knowledge and confidence about the interior structure of the Earth and with more computational power, it should be possible to predict small-scale plate motions.

3. Since the model presented here is dynamically self-consistent and can account for the normal forces across the plate boundaries, it will be useful for detailed study of intraplate stresses and mantle driving forces. The observation of intraplate deviatoric stress will place strong constraints on the dynamics of the mantle.

4. It is possible, by applying the model presented here, to realistically simulate self-consistent, time-dependent mantle convection and compare with geophysical and geological observations, such as, past plate reconstructions, sea level change, etc.

5. Concluding Remarks

1. We have provided a convective explanation for the present-day plate kinematic observations as well as for the toroidal/poloidal ratio. Large-scale plate motion is the result of mantle convection driven by internal density anomalies and modulated by extreme lateral variation of viscosity near the surface. Continental area, the distribution of "continents," and the length and distribution of subduction zones appear to be important in controlling the directions and magnitudes of the surface plate velocities. Convection can drive the plates at the right magnitudes and directions suggested by plate tectonic models.

2. The viscosity contrast between continental and oceanic regions, broadly defined, is the major control on the surface velocity field. Both layered mantle and whole mantle convection models, with continental regions having an effective integrated viscosity about 30-60 times larger than oceanic regions (assuming 90 km thick plates), are able to predict the correct patterns of surface poloidal and toroidal velocities and can account for the observed ratio of poloidal-toroidal motion. Weak asthenosphere tends to decouple the plates from the rest of the mantle and reinforces the generation of surface toroidal motion. To first order, large-scale mantle convection may be a very simple system governed by Newtonian or stress-dependent viscosity flow with radial and lateral variations of viscosity due to chemical or rheological differences.

3. The reference viscosity (corresponding to that of the 400 - 670 km depth interval) is 1.6 $\times$ 10^{21} Pa s assuming layered mantle flow and 3.2 $\times$ 10^{21} Pa s for whole mantle flow.

4. Mantle convection models, with lateral viscosity contrasts between continental and oceanic regions, predict very little net rotation of the lithosphere with respect to the rest of the mantle, which is not consistent with plate tectonic models using the hotspot reference frame.

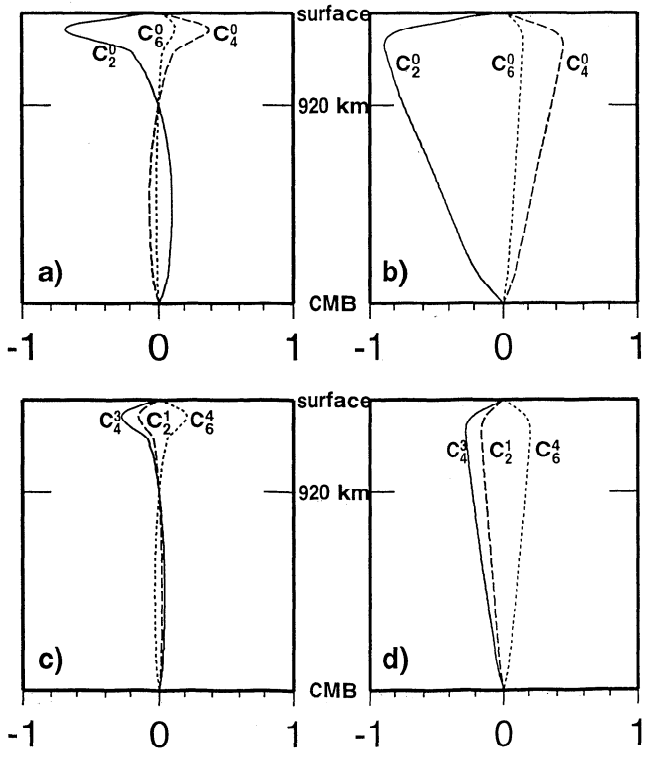

Figure 12. Kernels for surface poloidal and toroidal motions for a density load Y_2^0 in the mantle. The viscosity models are the same as those used in Figure 10.

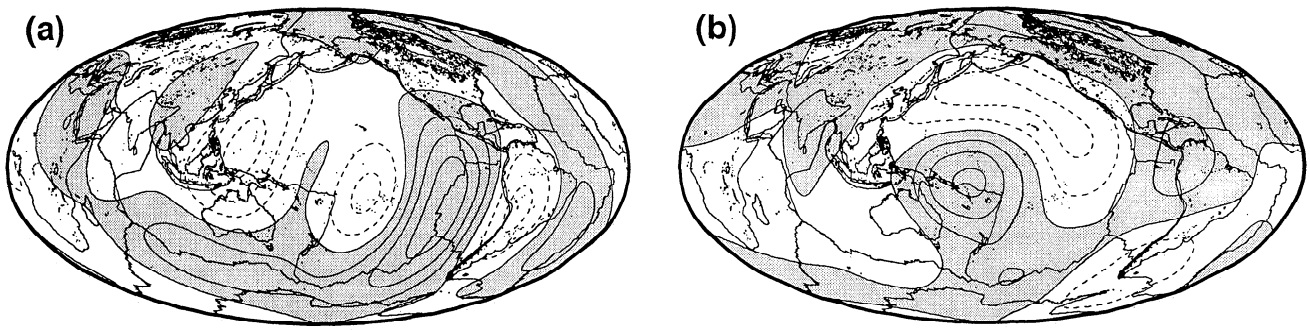

Figure 13. Same as those in Figures 10a and 10c for model LM, except that plate margins have the same viscosity as oceans, that is, only the viscosity contrast between "continents" and "oceans" is present in the upper 90 km.

Acknowledgments. We thank S. Zhang and M. Gurnis for helping us to check the code, S. Zhong for stimulating discussions and review. We also thank one anonymous associate editor of JGR for his/her insightful comments and an anonymous reviewer for useful suggestions. This work was funded by NSF grant EAR 92-18390. Contribution 5790, Division of Geological and Planetary Sciences, California Institute of Technology.

Appendix A: Newtonian Viscous Flow Formulations

Viscous flow in a self-gravitating fluid is governed by the equation of continuity, constitutive equations, and the equations of motion. In spherical coordinates the incompressible equation of continuity can be written [*Landau and Lifshitz*, 1959]

$$\frac{1}{r^2}\frac{\partial(r^2U_r)}{\partial r}+\frac{1}{r\sin\theta}\frac{\partial(U_\theta\sin\theta)}{\partial\theta}+\frac{1}{r\sin\theta}\frac{\partial U_\phi}{\partial\phi}=0 \quad \text{(A1)}$$

where U_r, U_θ and U_ϕ are three components of velocities in spherical coordinates.

The equations of motion, with variable viscosity, including self-gravitation and neglecting inertial effects, can be written in terms of the components of the deviatoric stress tensor as [*Landau and Lifshitz*, 1959]

$$-\frac{\partial P}{\partial r}+\rho\frac{\partial\Phi}{\partial r}+\frac{1}{r^2}\frac{\partial(r^2\tau_{rr})}{\partial r}+\frac{1}{r\sin\theta}\frac{\partial(\tau_{r\theta}\sin\theta)}{\partial\theta}+\frac{1}{r\sin\theta}\frac{\partial\tau_{r\phi}}{\partial\phi}-\frac{\tau_{\theta\theta}+\tau_{\phi\phi}}{r}-\delta\rho g_0=0 \quad \text{(A2)}$$

$$-\frac{1}{r}\frac{\partial P}{\partial\theta}+\rho\frac{1}{r}\frac{\partial\Phi}{\partial\theta}+\frac{1}{r^2}\frac{\partial(r^2\tau_{r\theta})}{\partial r}+\frac{1}{r\sin\theta}\frac{\partial(\tau_{\theta\theta}\sin\theta)}{\partial\theta}+\frac{1}{r\sin\theta}\frac{\partial\tau_{\theta\phi}}{\partial\phi}+\frac{\tau_{r\theta}}{r}-\frac{\cot\theta\tau_{\phi\phi}}{r}=0 \quad \text{(A3)}$$

$$-\frac{1}{r\sin\theta}\frac{\partial P}{\partial\phi}+\rho\frac{1}{r\sin\theta}\frac{\partial\Phi}{\partial\phi}+\frac{1}{r^2}\frac{\partial(r^2\tau_{r\phi})}{\partial r}+\frac{1}{r}\frac{\partial(\tau_{\theta\phi})}{\partial\theta}+\frac{1}{r\sin\theta}\frac{\partial\tau_{\phi\phi}}{\partial\phi}+\frac{\tau_{r\phi}}{r}+\frac{2\cot\theta\tau_{\theta\phi}}{r}=0 \quad \text{(A4)}$$

where, P is pressure, Φ is the perturbation of the gravitational potential, g_0 is gravitational acceleration, τ is the deviatoric stress tensor and $\delta\rho$ is the density perturbation.

The constitutive relationship between stress and velocities for a Newtonian fluid is

$$\tau_{r\theta}=\eta(-\frac{U_\theta}{r}+\frac{\partial U_\theta}{\partial r}+\frac{1}{r}\frac{\partial U_r}{\partial\theta}) \quad \text{(A5)}$$

$$\tau_{r\phi}=\eta(-\frac{U_\phi}{r}+\frac{\partial U_\phi}{\partial r}+\frac{1}{r\sin\theta}\frac{\partial U_r}{\partial\phi}) \quad \text{(A6)}$$

$$\tau_{rr}=2\eta\frac{\partial U_r}{\partial r} \quad \text{(A7)}$$

$$\tau_{\theta\theta}=2\eta(\frac{1}{r}\frac{\partial U_\theta}{\partial\theta}+\frac{U_r}{r}) \quad \text{(A8)}$$

$$\tau_{\phi\phi}=2\eta(\frac{1}{r\sin\theta}\frac{\partial U_\phi}{\partial\phi}+\frac{U_r}{r}+\frac{U_\theta\cot\theta}{r}) \quad \text{(A9)}$$

$$\tau_{\theta\phi}=\eta(-\frac{\cot\theta U_\phi}{r}+\frac{1}{r}\frac{\partial U_\phi}{\partial\theta}+\frac{1}{r\sin\theta}\frac{\partial U_\theta}{\partial\phi}) \quad \text{(A10)}$$

where $\eta=\eta(\theta,\phi)$ is the viscosity.

The three components of velocity and components of nonhydrostatic stress can be expressed as infinite series in terms of spherical harmonics $Y_{lm}(\theta,\phi)$:

$$U_r=Z_1^{lm}Y_{lm}(\theta,\phi) \quad \text{(A11)}$$

$$U_\theta=Z_2^{lm}Y_{lm}^{10}(\theta,\phi)+Z_5^{lm}Y_{lm}^{01}(\theta,\phi) \quad \text{(A12)}$$

$$U_\phi=Z_2^{lm}Y_{lm}^{01}(\theta,\phi)-Z_5^{lm}Y_{lm}^{10}(\theta,\phi) \quad \text{(A13)}$$

$$r(-P+\tau_{rr}+\rho\Phi)/\eta_0=Z_3^{lm}Y_{lm}(\theta,\phi) \quad \text{(A14)}$$

$$r(\tau_{r\theta})/\eta_0=Z_4^{lm}Y_{lm}^{10}(\theta,\phi)+Z_6^{lm}Y_{lm}^{01}(\theta,\phi) \quad \text{(A15)}$$

$$r(\tau_{r\phi})/\eta_0=Z_4^{lm}Y_{lm}^{01}(\theta,\phi)-Z_6^{lm}Y_{lm}^{10}(\theta,\phi) \quad \text{(A16)}$$

where Z_2^{lm} and Z_4^{lm} are the poloidal components of velocity and stress and Z_5^{lm} and Z_6^{lm} are the toroidal components of velocity and stress. Einstein summation convention is used and

$$Y_{lm}^{10}(\theta,\phi)=\frac{\partial Y_{lm}(\theta,\phi)}{\partial\theta}$$

$$Y_{lm}^{01}(\theta,\phi)=\frac{1}{\sin\theta}\frac{\partial Y_{lm}(\theta,\phi)}{\partial\phi}$$

Substituting (A11)-(A16) into (A1)-(A6) and taking each spherical harmonic by using the orthogonalities, after tedious algebra, we have the following equations:

$$\frac{\partial Z_1^{lm}}{\partial \mu} = -2Z_1^{lm} + LZ_2^{lm} \quad \text{(A17)}$$

$$\frac{\partial Z_2^{lm}}{\partial \mu} = -Z_1^{lm} + Z_2^{lm} + 1/\eta^* A_{lml'm'} Z_4^{l'm'} + 1/\eta^* B_{lml'm'} Z_6^{l'm'} \quad \text{(A18)}$$

$$\frac{\partial Z_3^{lm}}{\partial \mu} = 12\eta^* C_{lml'm'} Z_1^{l'm'} - 6L'\eta^* C_{lml'm'} Z_2^{l'm'} + Z_3^{lm} + LZ_4^{lm} + r^2 \delta\rho^{lm} g_0/\eta_0 \quad \text{(A19)}$$

$$\frac{\partial Z_4^{lm}}{\partial \mu} = -2Z_4^{lm} - Z_3^{lm} - 6\eta^* C_{lml'm'} Z_1^{l'm'} + \eta^* D_{lml'm'} Z_2^{l'm'} + \eta^* E_{lml'm'} Z_5^{l'm'} \quad \text{(A20)}$$

$$\frac{\partial Z_5^{lm}}{\partial \mu} = Z_5^{lm} - 1/\eta^* B_{lml'm'} Z_4^{l'm'} + 1/\eta^* A_{lml'm'} Z_6^{l'm'} \quad \text{(A21)}$$

$$\frac{\partial Z_6^{lm}}{\partial \mu} = -2Z_6^{lm} - \eta^* F_{lml'm'} Z_2^{l'm'} + \eta^* G_{lml'm'} Z_5^{l'm'} \quad \text{(A22)}$$

$$A_{lml'm'} = \frac{1}{L}\int\int \frac{1}{T(\theta,\phi)}(Y_{l'm'}^{10}(\theta,\phi)Y_{lm}^{*10}(\theta,\phi) + Y_{l'm'}^{01}(\theta,\phi)Y_{lm}^{*01}(\theta,\phi)) * ds$$

$$B_{lml'm'} = \frac{1}{L}\int\int \frac{1}{T(\theta,\phi)}(Y_{l'm'}^{01}(\theta,\phi)Y_{lm}^{*10}(\theta,\phi) - Y_{l'm'}^{10}(\theta,\phi)Y_{lm}^{*01}(\theta,\phi)) * ds$$

$$C_{lml'm'} = \int\int (T(\theta,\phi)Y_{l'm'}(\theta,\phi)Y_{lm}^{*}(\theta,\phi)) * ds$$

$$D_{lml'm'} = 2 * A1 + 4L'C_{lml'm'}$$

$$E_{lml'm'} = \frac{1}{L}(\int\int 2T(\theta,\phi)(L'Y_{l'm'}(\theta,\phi) + 2Y_{l'm'}^{20}(\theta,\phi)) * (\cot\theta Y_{lm}^{*01}(\theta,\phi) - Y_{lm}^{*11}(\theta,\phi)) - (\cot\theta Y_{l'm'}^{01}(\theta,\phi) - Y_{l'm'}^{11}(\theta,\phi)) * (LY_{lm}^{*}(\theta,\phi) + 2Y_{lm}^{*20}(\theta,\phi)) * ds$$

$$F_{lml'm'} = E_{lml'm'}$$

$$G_{lml'm'} = 2 * A1 + L'C_{lml'm'}$$

$$A1 = \frac{1}{L}(\int\int T(\theta,\phi)(L'Y_{l'm'}(\theta,\phi)Y_{lm}^{*20}(\theta,\phi) + L Y_{l'm'}^{20}(\theta,\phi)Y_{lm}^{*}(\theta,\phi) + 2Y_{l'm'}^{20}(\theta,\phi)Y_{lm}^{*20}(\theta,\phi) * ds + \int\int 2T(\theta,\phi)(Y_{l'm'}^{11}(\theta,\phi) - \cot\theta Y_{l'm'}^{01}(\theta,\phi)) * (Y_{lm}^{*11}(\theta,\phi) - \cot\theta Y_{lm}^{*01}(\theta,\phi)) * ds$$

where,

$$T(\theta,\phi) = \eta(\theta,\phi)/\overline{\eta}$$

$$\eta^* = \overline{\eta}/\eta_0$$

$$L = l(l+1)$$

$$L' = l'(l'+1)$$

$$\mu = \ln(\frac{r}{a})$$

where η_0 is the reference viscosity, $\overline{\eta}$ is the average viscosity in the shell and a is the radius of the Earth. Equation (A17) is derived from the continuity equation (A1); (A18) and (A21) come from constitutive relationship equations (A5) and (A6); (A19) comes from momentum equation (A2) and (A20) and (A22) come from momentum equations (A3) and (A4). Again Einstein summation convention is used.

Note that for a spherical shell with no lateral variation in viscosity, $T(\theta,\phi) = 1$, the coefficients $B_{lml'm'} = E_{lml'm'} = F_{lml'm'} = 0$, $A_{lml'm'} = C_{lml'm'} = \delta_{ll'}\delta_{mm'}$, $A1 = -\delta_{ll'}\delta_{mm'}$. The above equations are simplified to the identical equations in a radially symmetric structure [*Kaula*, 1975]. In that case, equations for each spherical harmonic are independent with those in other harmonics and they can be solved degree by degree.

For spherical shells with lateral variations in viscosity, the above equations are no longer separated by each mode, that is, modes are coupled with each other through those coupling coefficients $A_{lml'm'} - G_{lml'm'}$. Since the above summations go to infinity, we have no obvious way to solve these equations. However, if we truncate all the quantities up to a spherical harmonic degree ($l_{\max}$), that is, we neglect the coupling effects of spherical harmonic degrees $l > l_{\max}$, we have these linear equations by putting all the equations at degrees $l = 1 - l_{\max}$ together,

$$\frac{dZ}{d\mu} = B * Z + b; \quad \text{(A23)}$$

where,

$$Z = [Z_1^{10}...Z_6^{10}, ..., Z_1^{lm}...Z_6^{lm}]^T \quad \text{(A24)}$$

$$b = [0, 0, r^2 g\delta\rho^{10}/\eta_0, 0, 0, 0..., 0, 0, r^2 g\delta\rho^{lm}/\eta_0, 0, 0, 0]^T \quad \text{(A25)}$$

and B is a $3l_{\max}(l_{\max}+3) \times 3l_{\max}(l_{\max}+3)$ matrix with elements given by (A17)-(A22).

Appendix B: Propagator Matrix Method

In a shell, with same lateral variation in viscosity, the elements in B are constants. Equation (A23) can be solved by standard propagator matrix method. The solution of (A23) is

$$Z(\mu) = \exp[B(\mu-\mu_0)]Z(\mu_0) + \int_{\mu_0}^{\mu} \exp[B(\mu-\epsilon)]b(\epsilon)d\epsilon = P_B(\mu,\mu_0)Z(\mu_0) + \int_{\mu_0}^{\mu} P_B(\mu,\epsilon)b(\epsilon)d\epsilon \quad \text{(B1)}$$

The analysis can be simplified if $\delta\rho^{lm}(r)$ is approximated as a series of J discrete sheets or surface anomalies [*Hager and Clayton*, 1989]

$$\sigma_j^{lm} = \sum_{r_j-\epsilon}^{r_j+\epsilon} \delta\rho^{lm}(r)dr$$

Analogous to equation (4.40) of *Hager and Clayton* [1989], (B1) becomes

$$Z(\mu) = P_B(\mu,\mu_0)Z(\mu_0) + \sum_{j=1}^{J} P_B(\mu,\epsilon)b_j \quad \text{(B2)}$$

where

$$b_j = [0, 0, rg\sigma_j^{lm}/\eta_0, 0, 0, 0, ...0, 0, rg\sigma_j^{lm}/\eta_0, 0, 0, 0]^T \quad \text{(B3)}$$

The form of the propagator matrix P_B can be estimated in terms of its eigenvalues λ_i of matrix B. For example, for a matrix B with no repeated eigenvalues, the propagator matrix P_B is given by *Gantmacher* [1960]

$$P_B = \sum_{i=1} \exp[\lambda_i(\mu - \mu_0)] \prod_{s \neq i} (\lambda_s I - B)/(\lambda_s - \lambda_i) \quad \text{(B4)}$$

where I is the identity matrix.

When the dimension of matrix B is large, the above method is not practical, since it involves many matrix multiplications. When the thickness of the shell is small, P_B can be obtained directly from its definition with some approximations

$$\begin{aligned} P_B(\mu, \mu_0) &= \exp[B(\mu - \mu_0)] \\ &= I + \sum_{n=1}^{n=N} \frac{(\mu - \mu_0)^n}{n!} B^n \end{aligned} \quad \text{(B5)}$$

N is the truncated power. Numerical tests indicate that, for a shell with thickness of 20 km, P_B can be obtained within an error of 0.001% with $N = 4$.

Appendix C: Boundary Conditions

Velocities (U_r, U_θ, U_ϕ), stresses $(\tau_{rr}, \tau_{r\theta}, \tau_{r\phi})$ and Φ are continuous at any boundary in the mantle, that is, Z is continuous across any boundary. For boundary between layers with different viscosity but same intrinsic density, Z is continuous; for boundary in which intrinsic density changes (chemical boundary) and stratification of flow occurs, $Z_1^{lm} = 0$ $(U_r = 0)$, Z_3^{lm} has a jump of dZ_3^{lm}.

Shear tractions and vertical velocities at the CMB and surface are zero, simply because the viscosities in the atmosphere and core are negligible compared to that of the mantle. At the CMB,

$$\begin{aligned} Z(1) = [0, Z_2^{10}(1), Z_3^{10}(1), 0, Z_5^{10}(1), 0, \ ..., \\ 0, Z_2^{lm}(1), Z_3^{lm}(1), 0, Z_5^{lm}(1), 0]^T \end{aligned} \quad \text{(C1)}$$

$Z(1)$ is propagated to the surface of Earth by propagator matrices. At the surface of Earth, we have the boundary condition:

$$\begin{aligned} Z(0) = [0, Z_2^{10}(0), Z_3^{10}(0), 0, Z_5^{10}(0), 0, \ ..., \\ 0, Z_2^{lm}(0), Z_3^{lm}(0), 0, Z_5^{lm}(0), 0]^T \end{aligned} \quad \text{(C2)}$$

There are $3l_{\max}(l_{\max}+1)$ unknowns and $3l_{\max}(l_{\max}+1)$ linear equations for whole mantle flow, $7l_{\max}(l_{\max}+1)/2$ unknowns (one more (dZ_3^{lm}) for each spherical harmonic degree and order) and $7l_{\max}(l_{\max}+1)/2$ linear equations (one more $(U_r = 0)$ across the chemical boundary for each spherical harmonic degree and order) for layered flow.

References

Bercovici, D., A simple model of plate generation from mantle flow, *Geophys. J. Int.*, *114*, 635–650, 1993.

Bercovici, D., Plate generation in a simple model of lithosphere-mantle flow with dynamic self-lubrication, *Earth Planet. Sci. Lett.*, *144*, 41–51, 1996.

Cadek, O., Y. Ricard, Z. Martinec, and C. Matyska, Comparison between Newtonian and non-Newtonian flow driven by internal loads, *Geophys. J. Int.*, *112*, 103–114, 1993.

Cazenave, A., A. Souriau, and K. Dominh, Global coupling of the Earth surface topography with hotspots, geoid and mantle heterogeneity, *Nature*, *340*, 54–57, 1989.

Christensen, U. R., and H. Harder, 3-D convection with variable viscosity, *Geophys. J. Int.*, *104*, 213–226, 1991.

Forte, A. M., and W. R. Peltier, Plate tectonics and aspherical Earth structure: The importance of poloidal-toroidal coupling, *J. Geophys. Res.*, *92*, 3645–3679, 1987.

Forte, A. M., and W. R. Peltier, Viscous flow models of global geophysical observables, 1, Forward problems, *J. Geophys. Res.*, *96*, 20131–20159, 1991.

Forte, A. M., A. M. Dziewonski, and R. L. Woodward, Aspherical structure of the mantle tectonics, nonhydrostatic geoid and the topography of the core-mantle boundary, in *Dynamics of the Earth's Deep Interior and Earth Rotation*, Geophys. Monogr Ser., edited by J. L. Mouel, D. E. Smylie, and T. Herring, vol. 72, pp. 135–166, Washington, D. C., 1993.

Gable, C. W., R. J. O'Connell, and B. J. Travis, Convection in three dimensions with surface plates: Generation of toroidal flow, *J. Geophys. Res.*, *96*, 8391–8405, 1991.

Gantmacher, F. R., The Theory of Matrices, vol. 2, translated from Russian by K. A. Hirsch, Chelsea, New York, 1960.

Gordon, R. G., and D. M. Jurdy, Cenozoic global plate motions, *J. Geophys. Res.*, *91*, 12389–12406, 1986.

Grand, S. P., Mantle shear structure beneath the Americas and surrounding oceans, *J. Geophys. Res.*, *99*, 11591 – 11622, 1994.

Gurnis, M., A reassessment of the heat transport by variable viscosity convection with plates and lids, *Geophys. Res. Lett.*, *16*, 179–182, 1989.

Hager, B. H., Subducted slabs and the geoid: Constraints on mantle rheology and flow, *J. Geophys. Res.*, *89*, 6003–6015, 1984.

Hager, B. H., and R. W. Clayton, Constraints on the structure of mantle convection using seismic observations, flow models, and the geoid, in *Mantle Convection*, edited by W. R. Peltier, pp. 657–764, Gordon and Breach, Newark, N. J., 1989.

Hager, B. H., and R. J. O'Connell, Kinematic models of large-scale flow in the Earth's mantle, *J. Geophys. Res.*, *84*, 1031–1048, 1979.

Hager, B. H., and R. J. O'Connell, A simple global model of plate dynamics and mantle convection, *J. Geophys. Res.*, *86*, 4843–4878, 1981.

Hager, B. H., R. W. Clayton, M. A. Richards, R. P. Comer, and A. M. Dziewonski, Lower mantle heterogeneity, dynamic topography and the geoid, *Nature*, *313*, 541–545, 1985.

Heestand, R. L., and S. T. Crough, The effect of hotspots on the oceanic age-depth relation, *J. Geophys. Res.*, *86*, 6107–6114, 1981.

Kaula, W. M., Product-sum conversion of spherical harmonics with application to thermal convection, *J. Geophys. Res.*, *80*, 225–231, 1975.

Lachenbruch, A. H., and J. H. Sass, The stress heat-flow paradox and thermal results from Cajon Pass, *Geophys. Res. Lett.*, *15*, 981–984, 1988.

Landau, L. D., and E. M. Lifshitz, Fluid Mechanics, p. 536, Pergamon, New York, 1959.

Lithgow-Bertelloni, C., and M. A. Richards, Cenozoic plate driving forces, *Geophys. Res. Lett.*, *22*, 1317–1320, 1995.

Minster, J. B., and T. Jordan, Present-day plate motions, *J. Geophys. Res.*, *83*, 5331–5354, 1978.

Müller, R. D., W. R. Roest, J.-Y. Royer, L. M. Gahagan, and J. G. Sclater, A digital age map of the ocean floor, in *SID Reference Series*, pp. 93–303, Scripps Inst. of Oceanogr., Univ. of Calif., San Diego, La Jolla, 1993.

O'Connell, R. J., C. W. Gable, and B. H. Hager, Toroidal-poloidal partitioning of lithospheric plate motion, in *Glacial Isostasy, Sea Level and Mantle Rheology*, edited by K. L. R. Sabadini and E. Boshci, pp. 513–535, Kluwer, Acad., Norwell, Mass., 1991.

Olsen, P., and D. Bercovici, On the equipartitioning of kinetic energy in plate tectonics, *Geophys. Res. Lett.*, *18*, 1751–1754, 1991.

Parsons, B. E., and J. G. Sclater, An analysis of the variation of ocean floor bathymetry and heat flow with age, *J. Geophys. Res.*, *82*, 803–827, 1977.

Polet, J., and D. L. Anderson, Depth extent of cratons as inferred from tomographic studies, *Geology*, *23*, 205 – 208, 1995.

Ribe, N., The dynamics of thin shell with variable viscosity and the origin of toroidal flow in the mantle, *Geophys. J. Int.*, *110*, 537–552, 1992.

Ricard, Y., and C. Vigny, Mantle dynamics with induced plate tectonics, *J. Geophys. Res.*, *94*, 17543–17559, 1989.

Ricard, Y., L. Fleitout, and C. Froidevaux, Geoid heights and lithospheric stresses for a dynamic Earth, *Ann. Geophys.*, *2*, 267–286, 1984.

Ricard, Y., C. Froidevaux, and L. Fleitout, Global plate motions and the geoid: A physical model, *Geophys. J. Int.*, *93*, 477–484, 1988.

Ricard, Y., C. Doglioni, and R. Sabadini, Differential rotation between lithosphere and mantle: A consequence of lateral mantle viscosity variation, *J. Geophys. Res.*, *96*, 8407–8415, 1991.

Richards, M. A., and B. H. Hager, Effects of lateral viscosity variations on long-wavelength geoid anomalies and topography, *J. Geophys. Res.*, *94*, 10299–10313, 1989.

Richter, F., Dynamic models for sea floor spreading, *Rev. Geophys.*, *11*, 223–287, 1973.

Schubert, G., C. Froidevaux, and D. A. Yuen, Oceanic lithosphere and asthenosphere: Thermal and mechanical structure, *J. Geophys. Res.*, *81*, 3525–3540, 1976.

Stein, C. A., and S. Stein, A model for the global variation in oceanic depth and heat flow with lithospheric age, *Nature*, *359*, 123–129, 1992.

Stewart, C. A., Thermal convection in the Earth's mantle: Mode coupling induced by temperature-dependent viscosity in a three-dimensional spherical shell, *Geophys. Res. Lett.*, *19*, 337–340, 1992.

Su, W. J., R. L. Woodward, and A. M. Dziewonski, Degree 12 model of shear velocity heterogeneity in the mantle, *J. Geophys. Res.*, *99*, 6945–6980, 1994.

Tackley, P. J., Effects of strongly temperature-dependent viscosity on time-dependent three-dimensional models of mantle convection, *EOS Trans. AGU*, *74*, *F(43)*, Fall Meet. Suppl., 79, 1993.

Turcotte, D. L., and E. R. Oxburgh, Finite amplitude convective cells and continental drift, *J. Fluid Mech.*, *28*, 29–42, 1967.

Wen, L., and D. L. Anderson, Slabs, hotspots, cratons and mantle convection revealed from residual seismic tomography in the upper mantle, *Phys. Earth Planet. Inter.*, *99*, 131–143, 1997a.

Wen, L., and D. L. Anderson, Layered mantle convection: A model for geoid and topography, *Earth Planet. Sci. Lett.*, *146*, 367–377, 1997b.

Zhang, S., and U. R. Christensen, Some effects of lateral viscosity variations on geoid and surface velocities induced by density anomalies in the mantle, *Geophys. J. Int.*, *114*, 531–547, 1993.

Zhang, Y. S., and T. Tanimoto, High-resolution global upper mantle structure and plate tectonics, *J. Geophys. Res.*, *98*, 9790–9823, 1993.

Zhong, S., and M. Gurnis, Mantle convection with plates and mobile, faulted plate margins, *Science*, *267*, 838–843, 1995.

Zhong, S., and M. Gurnis, Interaction of weak faults and non-newtonian rheology produces plate tectonics in a 3D model of mantle flow, *Nature*, *385*, 245–247, 1996.

L. Wen and D. L. Anderson, Seismological Laboratory, California Institute of Technology, Pasadena, CA 91125. (e-mail: wen@gps.caltech.edu)

(Received December 11, 1996; revised July 14, 1997; accepted July 29, 1997.)